

Article

# Hyperfine Structure and Isotope Shifts in Dy II

Dylan F. Del Papa, Richard A. Holt and S. David Rosner \*

Department of Physics & Astronomy, University of Western Ontario, London, ON N6A 3K7, Canada; ddelpapa@uwo.ca (D.F.D.P.); rholt@uwo.ca (R.A.H.)

\* Correspondence: rosner@uwo.ca

Academic Editor: Joseph Reader

Received: 8 December 2016; Accepted: 13 January 2017; Published: 20 January 2017

**Abstract:** Using fast-ion-beam laser-fluorescence spectroscopy (FIBLAS), we have measured the hyperfine structure (hfs) of 14 levels and an additional four transitions in Dy II and the isotope shifts (IS) of 12 transitions in the wavelength range of 422–460 nm. These are the first precision measurements of this kind in Dy II. Along with hfs and IS, new undocumented transitions were discovered within 3 GHz of the targeted transitions. These atomic data are essential for astrophysical studies of chemical abundances, allowing correction for saturation and the effects of blended lines. Lanthanide abundances are important in diffusion modeling of stellar interiors, and in the mechanisms and history of nucleosynthesis in the universe. Hfs and IS also play an important role in the classification of energy levels, and provide a benchmark for theoretical atomic structure calculations.

**Keywords:** laser spectroscopy; ionized atoms; hyperfine structure; isotope shifts

## 1. Introduction

Accurate elemental abundances in stars and the interstellar medium are essential for understanding stellar formation, evolution, and structure. Deriving abundances from stellar spectra requires accurate atomic data: tabulated spectra of several ionization states (usually I–III), oscillator strengths, hyperfine structure (hfs), and isotope shifts (IS). Even though hfs and IS are too small to be resolved in most astrophysical spectra because of Doppler and rotational broadening, they contribute to the overall profile of a spectral line; extracting the elemental abundance from a line often requires a knowledge of the hfs to correct for saturation [1], and ignoring the underlying structure arising from hfs and IS can lead to errors as large as two to three orders of magnitude [2]. In addition, there can be errors in the determination of rotational, microturbulent and macroturbulent velocities from Fourier analysis of line profiles, and unknown shifts in wavelengths of saturated lines [3]. The lanthanides are particularly important because they provide a contiguous sequence of observable elements in which patterns of abundance may be observed and related to nucleosynthesis and chemical fractionation [4]. In this paper, we present new measurements of hfs and IS in Dy II, one of the lanthanide elements that is used to understand these processes.

The main mechanisms of neutron capture by which elements beyond  $^{56}\text{Fe}$  are formed are the *r*-process and *s*-process, named by whether the rate of neutron capture is rapid or slow compared to the rate of  $\beta$ -decay [5]. The *s*-process is believed to take place in thermally pulsing asymptotic giant branch (AGB) stars [6], whereas the *r*-process requires the high neutron density characteristic of supernovas. Comparison of the elemental composition of a star with theoretical *r*- or *s*-process models gives information about the nature of these processes and about the environment in which the star formed. The observed ratio of the abundances of a pair of unstable and stable *r*-process elements, e.g.,  $[\text{Th}]/[\text{Eu}]$ , can yield the age of the star when compared with the theoretical production ratio [7]. There are several recent studies of abundances in very metal-poor stars, which are believed to have

formed from the debris of the very first generation of initially metal-free massive stars (Population III). These studies shed light on the earliest nucleosynthesis of heavy elements in the universe and how they were incorporated into later stars [8,9]. CH stars, which are deficient in Fe and enhanced in C and s-process elements, obtained their heavy elements by mass transfer from now-unseen white dwarf binary companions when the latter were in the AGB stage of evolution. Thus the composition of CH stars reveals information about AGB synthesis of s-process elements [10].

Accurate abundance information is also required in the study of diffusion processes within stars, where chemical fractionation occurs due to a combination of gravity, convection and radiation pressure. The chemically peculiar (CP) stars exhibit typically large lanthanide abundance excesses relative to solar and meteoritic values, and the abundance pattern expected from nucleosynthesis may be greatly perturbed [4]. One of the most exciting recent developments in stellar astrophysics has been the rapid expansion of the field of asteroseismology [11], in which the observation of natural, resonant oscillations provides information about stellar interiors and evolution. These observations can be photometric or velocity measurements from Doppler shifts. In the latter case, it is essential to be able to model spectral line shapes accurately, requiring good atomic data.

Extensive spectroscopy of Dy II has been done principally by Conway and Worden [12], Wyart [13–15], and more recently by Nave and Griesmann [16], who pointed out the complexity of lanthanide spectra due to the large number of terms arising from the unfilled 4*f* shell and the fact that 4*f*, 5*d*, and 6*s* electrons all have similar binding energies. The NIST Atomic Spectra Database [17] lists 576 levels of which a significant number are only partly classified as to principal configuration and term, and configuration mixing is common. One of the tools that has been used to aid in level classification is IS, since the ‘field shift’ part of the IS (the dominant contribution in heavy atoms) depends on the electron density at the nucleus and therefore is a function of the electronic states involved in a transition. Early measurements of IS were carried out by Pacheva and Abadjieva [18]. Aufmuth [19] measured IS for Dy isotopes 162–164 in 29 lines of Dy II in order to check the mixing of three configurations calculated by Wyart [13–15]. Ahmad et al. [20] measured the IS of 62 spectral lines, three of which overlap with our measurements. The only previous report of hfs is by Murakawa and Kamei [21].

## 2. Experimental Setup

The FIBLAS method [22] we use is very well suited to the measurement of the detailed structure within an atomic transition because of the high spectral resolution (full-width-half-maximum linewidths of ~100 MHz), the high wavelength selectivity of a narrow-band laser, and the ability to mass-select the targeted ions in the fast beam. The transition linewidths are a combination of the natural width (here 20–70 MHz), and Doppler broadening from the ion source, significantly narrowed for fast ions by ‘kinematic compression’ [23]. The hfs and IS of an optical transition are often completely resolved, a goal difficult to achieve in other techniques, such as Fourier transform spectroscopy.

In our apparatus, Dy<sup>+</sup> ions are created using a Penning sputter ion source, engineered by us to yield a small energy spread of a few eV in the extracted beam [24,25]. Another important feature is the large population of metastable ions in the beam with energies up to ~22,000 cm<sup>-1</sup>, greatly enhancing the number of transitions we can observe. The use of sputtering rather than thermal evaporation makes the source universal for any solid conducting element in the periodic table; this is a great advantage for the lanthanides and many other refractory metals of astrophysical importance. A discharge in the Ne support gas is easily struck at anode-cathode potentials of several hundred volts, with the discharge current regulated at 60 mA. Our experience with lanthanides is that there is an initial period of conditioning (up to 2 h), during which the potential drops to ~200–300 V, and the extracted ion current, as measured in a downstream Faraday cup, rises sharply to ~200 nA. We attribute this behavior to sputter-cleaning of the surfaces of the lanthanide cathode and anticathode to remove oxide layers, which form easily in air.

After initial acceleration to energies of 10–12 keV, the ion beam is focused by an einzel lens, steered, and mass-selected using a Wien filter. Removal of the large Ne<sup>+</sup> current from the beam reduces space-charge spreading and significantly lowers the collision-induced background fluorescence. The mass resolution of the Wien filter was selected by adjustment of its electric field to reject the Ne ions, while transmitting nearly equally the seven stable isotopes of Dy (see Table 1) to allow IS measurement. The mass-selected beam is then horizontally deflected by 5° to make it collinear with the laser beam. After further focusing and steering, the ions are accelerated by 478 eV into a ‘Doppler tuning’ region; this energy boost ensures the laser-induced fluorescence (LIF) is mainly confined to this region, from which it is transmitted out of the vacuum chamber by an array of optical fibers to a photomultiplier equipped with a short-pass filter. The filter allows rejection of the scattered laser light while transmitting most of the LIF, since the lower (metastable) energy states of the laser-induced transitions we observed ranged from ~4300 cm<sup>-1</sup> to 22,000 cm<sup>-1</sup>.

**Table 1.** Properties of the Dy isotopes.  $I$ ,  $\mu$ , and  $Q$  are the nuclear spin, magnetic dipole moment, and electric quadrupole moment, respectively.

Isotope	Mass (u) <sup>a</sup>	Abundance (%) <sup>b</sup>	$I$ <sup>c</sup>	$\mu$ (nm) <sup>c</sup>	$Q$ (b) <sup>c</sup>
<sup>156</sup> Dy	155.924278	0.06	0		
<sup>158</sup> Dy	157.924405	0.10	0		
<sup>160</sup> Dy	159.925194	2.34	0		
<sup>161</sup> Dy	160.926930	18.91	5/2	-0.480 (3)	+2.51 (2)
<sup>162</sup> Dy	161.926795	25.51	0		
<sup>163</sup> Dy	162.928728	24.90	5/2	+0.673 (4)	+2.318 (6)
<sup>164</sup> Dy	163.929171	28.18	0		

<sup>a</sup> Reference [26]; <sup>b</sup> Reference [27]; <sup>c</sup> Reference [28].

The laser system is a single-mode ring dye laser operating with Stilbene 420 dye, whose usable output range is ~420 nm to 460 nm. It is pumped with the all-lines UV output of an Ar-ion laser, and is frequency stabilized to a few MHz. The dye laser wavelength is monitored to ~1 part in 10<sup>7</sup> by a traveling-mirror Michelson interferometer [29] using a polarization-stabilized HeNe laser as a reference. The laser beam is loosely focused to a waist located approximately in the Doppler-tuning region. Before starting the laser scan across the hfs/IS components of a transition, the laser frequency is manually tuned to the absorption line of <sup>162</sup>Dy, which is the even isotope (i.e., without hfs) closest to the mean mass of the stable isotopes. The overlap of the laser and ion beams is optimized by adjusting steering and focusing of the ion beam. This results in a scan where the peak intensities of the even isotopes approximately match their standard abundances, facilitating subsequent analysis of the spectrum. During the scan, a computer steps the laser frequency over the entire spectrum of the line (<20 GHz) in intervals of ~1/10th of a linewidth with a dwell time of typically 250 ms. The computer simultaneously records the LIF signal along with the ion beam current, laser beam power, and a calibration signal that corrects for the nonlinearity (~2%) of the laser scan. This calibration signal is obtained using a set of markers generated by a plane-parallel Fabry-Perot interferometer with a free spectral range of 665.980 MHz, which is used to convert channel number into laser frequency difference.

Because the Dy II hfs is complicated by the existence of an unusually large electric quadrupole interaction, we introduced some redundancy to the data in order to allow checks on the robustness of the analysis. This was done by taking spectra with the laser beam both parallel (P) and antiparallel (A) to the ion beam, and by changing the ion-beam energy. Both of these measures change the large Doppler shift for each isotope, resulting in significant changes in the appearance of the measured spectrum. This can result in a P (or A) spectrum that is much less congested than its counterpart, greatly facilitating the analysis (see below).

### 3. Data and Analysis

A typical spectrum with fully resolved hfs and IS is shown in Figure 1, in which the ‘stick figure’ below the data shows the fitted peak locations. At the left of the figure, a number of peaks belonging to another, weaker transition can be seen. The spectra in which such blends occurred are noted in the IS table below by asterisks. The relative intensities of the extra transitions ranged from 1% to 15%, except in the case of the 443.100 nm line, for which two nearly equal-intensity transitions were seen, precluding analysis. The peaks corresponding to  $^{156}\text{Dy}$  and  $^{158}\text{Dy}$  were too small to be seen above the noise in our spectra and were not included in the analysis.

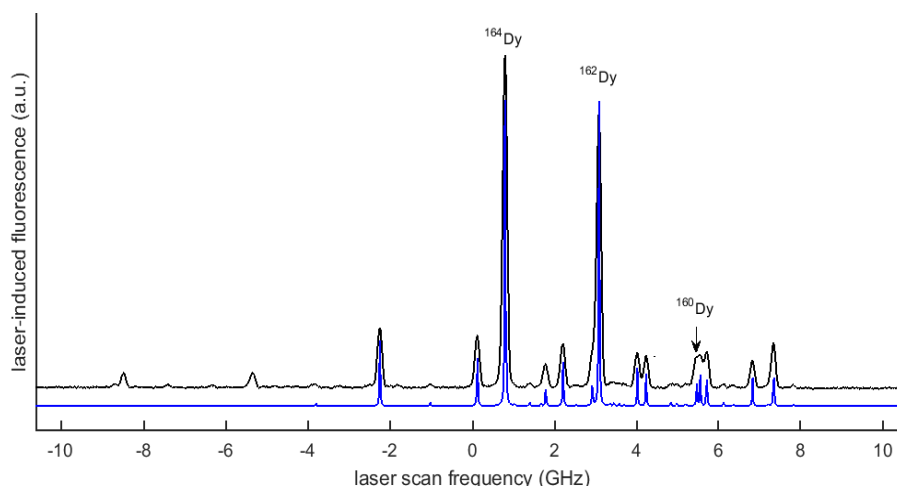


**Figure 1.** Laser-induced fluorescence spectrum of the transition  $4f^{10}(^5I_6)6s_{1/2}(6, 1/2)_{13/2} - 4f^{10}(^5I)6p^o_{13/2}$  at 438.430 nm in Dy II. The laser beam and ion beam were in parallel geometry. The observed spectrum (upper curve) is a single scan of 1024 channels at a dwell time of 400 ms per channel. The photomultiplier signal current for the  $^{164}\text{Dy}$  peak was  $\sim 80$  nA on a background of  $\sim 10$  nA due to collisionally-induced light. The observed FWHM linewidth was 98.8 MHz, which includes the 10.6 MHz natural width. The lower ‘stick figure’ (blue online) shows the positions and amplitudes of the fitted components, and has been displaced vertically for clarity. The hfs components of  $^{161}\text{Dy}$  and  $^{163}\text{Dy}$  are not individually annotated. It is important to understand that the separations between peaks of different isotopes arise from a combination of IS and relative Doppler shift. Note that the components of a second, partially blended, transition are visible on the left side.

Figure 2a,b show another transition observed in both P and A modes to demonstrate the ‘decongestion’ that occurs in one of these modes.

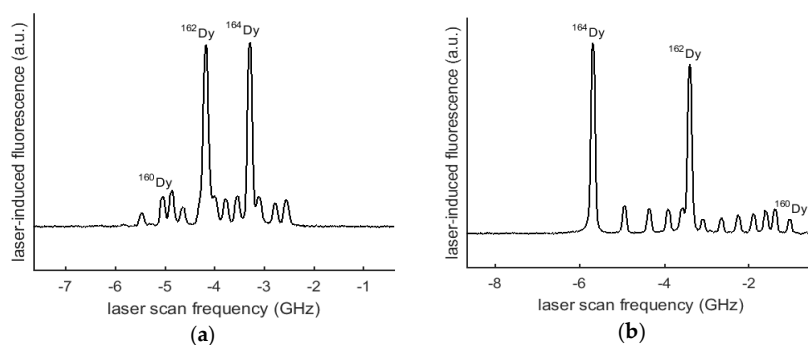


**Figure 2.** Laser-induced fluorescence spectrum of the transition  $4f^9(^6H^o)5d(^7I^o)6s^8I_{17/2}^o - 4f^9(^6H^o)5d(^7H^o)6p_{15/2}$  at 436.135 nm in Dy II, showing the advantage of viewing the same transition in two different laser beam/ion beam geometries: (a) Anti-parallel; (b) Parallel.

It is important to note that in the large separation  $\Delta\nu_\ell$  any pair of peaks corresponding to two different isotopes shown in these spectra is predominantly a *differential Doppler shift* arising from the slightly different velocity of each isotope. In the A (P) mode, driving a transition whose rest-frame frequency is  $\nu_0$  requires a laser frequency  $\nu_\ell$  given by

$$\nu_\ell = \nu_0 \left( \frac{1 \mp \beta}{1 \pm \beta} \right)^{1/2} \quad (1)$$

where  $\beta = (2eV/Mc^2)^{1/2}$  for a singly-charged ion of mass  $M$  accelerated from rest through a potential difference  $V$ . Thus, the ion-rest-frame peak separation  $\Delta\nu_0$  (which is the IS within a sign) for a pair of masses  $M$  and  $M'$  is related to  $\Delta\nu_\ell$  by

$$\Delta\nu_\ell = \Delta\nu_0 \left( \frac{1 \mp \beta'}{1 \pm \beta'} \right)^{1/2} + \nu_0 \left[ \left( \frac{1 \mp \beta'}{1 \pm \beta'} \right)^{1/2} - \left( \frac{1 \mp \beta}{1 \pm \beta} \right)^{1/2} \right] \quad (2)$$

(This formula may also be applied to the separation of a pair of hf peaks of the same mass by setting  $\beta' = \beta$ .) Creating the model spectrum to be fit to the data thus requires knowledge of the kinetic energy of the fast ions, which depends on the potential in the ion source, the extraction voltage, and the potential in the Doppler-tuning region. It is possible to determine the beam energy directly by measuring the Doppler-shifted wavenumber of a given spectral line in both A and P modes; a simple calculation with Equation (1) yields the velocity of the isotope corresponding to that spectral line as well as the transition wavenumber in the ion rest frame. Such measurements have shown that the beam energy is, within  $\sim 1$  eV, just the sum of the anode-cathode potential difference  $V_{ac}$  (the power-supply potential difference  $V_{supply}$  minus the 58.5 V drop across a 1 k $\Omega$  stabilizing ballast resistor) and the 10 kV or 12 kV extraction voltage, minus the potential in the central region of the Doppler-tuning region ( $-478$  V), determined from its applied voltage using a numerical solution of Laplace's equation. This implies that the plasma region in which the ions are created is at the potential of the anode. In order to account for the Doppler shifts in a spectrum, we thus needed to monitor only  $V_{supply}$  during the few minutes of a scan. Typically,  $V_{supply}$  varied by  $<1$  V in the current-regulated plasma, and only such scans were used as data.

The model used in the least-squares fit makes use of the standard formula [30] for the hyperfine contribution to the energy of a level with a nuclear spin  $I$ , an electronic angular momentum  $J$ , and a total angular momentum  $F$ , containing magnetic-dipole and electric-quadrupole terms, with parameters  $A$  and  $B$ , respectively:

$$\nu_{\text{hfs}}(F) = \frac{1}{2}AK + \frac{1}{2}B \frac{3K(K+1) - 4I(I+1)J(J+1)}{2I(2I-1)2J(2J-1)} \quad (3)$$

where  $K = F(F+1) - I(I+1) - J(J+1)$ . The amplitudes of the model peaks are constrained by the standard abundances of the isotopes, and, also, for the odd isotopes displaying hfs, by standard angular momentum recoupling coefficients:

$$a(F, F') \propto (2I+1)^{-1}(2F+1)(2F'+1) \left\{ \begin{matrix} F' & F & 1 \\ J & J' & I \end{matrix} \right\}^2 \quad (4)$$

where the primes (non-primes) indicate the upper (lower) level of a transition. A further constraint was the use of known ratios (see Table 1) of the nuclear magnetic moments and electric quadrupole moments of the odd isotopes  $^{161}\text{Dy}$  and  $^{163}\text{Dy}$ , so that the hfs of only one isotope needed to be fit. We are thus neglecting the hyperfine anomaly, which is expected to be small compared to our measurement uncertainty. The experimental lineshapes combine natural broadening with asymmetric Doppler broadening, arising mainly from the unknown potential distribution in the source plasma; we interpret the 'tail' of slower-energy ions as those created in the 'cathode fall' region. In the course

of data analysis, we observed that an asymmetric Lorentzian profile improved the consistency of the data. We note that the peak frequency *differences* determining the IS and hfs constants are insensitive to the detailed lineshape model used.

In addition to the four observable IS (measured with  $^{164}\text{Dy}$  as the reference) and four hfs constants for a given transition, other adjustable parameters in the fit included the overall frequency offset, overall amplitude, background, linewidth, asymmetry, and laser power (to account for saturation). The large electric quadrupole contribution to the hfs created splittings very different from the standard ‘flag’ pattern obtained when the magnetic dipole interaction dominates. Without the help of pattern recognition, it was necessary to use trial and error along with global fitting algorithms, searching across up to six parameters to find a fit. Another issue was that the pattern of a spectrum was dependent mainly on the differences  $B'-B$  and  $A'-A$ , with only subtle changes in the fit spectrum resulting from varying the *individual* values of the constants. Thus, as an intermediate measure, the search space could be reduced by fixing the constants associated with either the lower or upper energy level. A very important factor in breaking these parameter correlations is the ability to measure the relatively weak satellite peaks ( $\Delta F \neq \Delta J$ ) in the hyperfine spectra, since the frequencies of these peaks depend algebraically on the four hfs constants rather differently than for the principal peaks ( $\Delta F = \Delta J$ ). We also dealt with these correlations experimentally by repeating measurements of most transitions at different beam energies (10 keV and 12 keV) and different relative beam orientations (A and P modes). In four cases, the satellite peaks were not visible, with the result that the associated hfs constants were not individually well-determined, but are rather to be regarded as a set of ‘effective’ parameters that reproduce the principal peaks of the observed spectrum very well so as to be of practical use in modeling astrophysical spectra.

The resulting hfs constants for six lower and eight upper levels are given in Table 2, while Table 3 lists the effective hfs parameters for the four transitions referred to above. For the levels listed in Table 2, we were able to use several transitions to determine the hfs constants in each case, providing important ‘cross-checks’; however, the levels in Table 3 were only accessible using the transitions listed.

**Table 2.** Hyperfine structure constants of levels of  $^{161}\text{Dy}$  II and  $^{163}\text{Dy}$  II derived from transitions where satellite peaks are well fit.  $A$  and  $B$  are the magnetic dipole and electric quadrupole constants, respectively.  $J$  is the total angular momentum. Energies of odd-parity levels are italicized.

Configuration <sup>a</sup>	Term <sup>a</sup>	$J$ <sup>a</sup>	Energy <sup>a</sup> ( $\text{cm}^{-1}$ )	$A$ ( $^{161}\text{Dy}$ ) (MHz)	$B$ ( $^{161}\text{Dy}$ ) (MHz)	$A$ ( $^{163}\text{Dy}$ ) (MHz)	$B$ ( $^{163}\text{Dy}$ ) (MHz)
$4f^{10}(^5\text{I}_7)6s_{1/2}$	(7, 1/2)	15/2	4341.104	−251.89 (94)	1045 (48)	352.6 (1.3)	1104 (46)
$4f^{10}(^5\text{I}_6)6s_{1/2}$	(6, 1/2)	13/2	7485.117	93.22 (16)	−883.4 (7.1)	−130.48 (22)	−933.1 (7.5)
$4f^{10}(^3\text{F}_5)6s_{1/2}$	(5, 1/2)	11/2	13,338.27	−272.49 (23)	−818 (10)	381.44 (32)	−864 (11)
$4f^9(^6\text{H}^\circ)5d(^7\text{K}^\circ)6s$	$^8\text{K}^\circ$	19/2	17,606.65	−144.40 (30)	4081 (17)	202.13 (41)	4310 (18)
$4f^9(^6\text{H}^\circ)5d(^7\text{K}^\circ)6s$	$^6\text{K}^\circ$	19/2	19,571.75	−69.51 (35)	3861 (24)	97.29 (49)	4078 (25)
$4f^9(^6\text{H}^\circ)5d(^3\text{F})$	°	11/2	20,517.39	−96.98 (37)	2076 (17)	135.76 (52)	2193 (18)
$4f^9(^6\text{H}^\circ)5d(^3\text{P})$	°	15/2	27,435.132	−97.23 (12)	252.8 (7.1)	136.10 (17)	267.1 (7.5)
$4f^9(^6\text{H}^\circ)5d(^3\text{F})$	°	13/2	28,019.70	−114.76 (56)	1104 (37)	159.67 (78)	1166 (39)
$4f^{10}(^5\text{I})6p$	°	13/2	30,287.36	278.44 (18)	−973.9 (7.3)	−389.76 (25)	−1028.6 (7.7)
	°	9/2	36,466.34	−110.97 (24)	801 (14)	155.34 (33)	846 (15)
$4f^9(^6\text{H}^\circ)6s6p(^3\text{P}^\circ)$		17/2	40,455.73	−165.08 (32)	3851 (17)	231.08 (44)	4067 (18)
$4f^9(^6\text{H}^\circ)5d(^7\text{H}^\circ)6p$		17/2	41,583.90	−102.69 (31)	1826 (18)	143.75 (43)	1929 (19)
$4f^9(^6\text{H}^\circ)5d(^7\text{H}^\circ)6p$		13/2	42,289.33	−96.92 (45)	2773 (38)	135.67 (63)	2929 (40)
$4f^9(^6\text{H}^\circ)5d(^7\text{H}^\circ)6p$		19/2	42,478.98	−113.16 (42)	3099 (24)	158.40 (59)	3273 (26)

<sup>a</sup> Reference [17].

Table 4 presents the IS for 12 transitions, using the standard sign convention that  $IS \equiv \nu_{M'} - \nu_M$  where  $M' > M$ . The uncertainties in the data arise from the curve-fitting procedure, the residual non-linearity of the laser scan, and small drifts in  $V_{ac}$ . Equation (2) can be used to calculate the sensitivity of the measured separation  $\Delta\nu_\ell$  of two spectral peaks to the accuracy of the ion-beam energy eV, and to drifts in that energy *during a scan*. If the drift is zero,  $d(\Delta\nu_\ell)/dV$  is completely negligible for two hyperfine (hf) peaks of the same mass, and is  $\sim 0.15$  MHz/V for peaks of the isotope pair (160, 164).

Since we know  $V$  to  $\sim 1$  V, this effect is negligible compared to fitting errors. If the drift is non-zero, the sensitivity for any pair of peaks is  $\sim 12$  MHz/V for typical values of  $\nu_0$  and the beam energy. For the hf spectrum of a given isotope, the effect of a drift is taken into account by the fitting error since the many hf peaks are fit with only four hf parameters. For the same reason any residual non-linearity in the frequency scale is also subsumed in the fitting error. However, drift in  $V$  can contribute an error to the IS data, just as non-linearity can. Accordingly, we have added a contribution to the error budget of the IS of 10 MHz to account for both of these effects. We present evidence (see below) that this estimate is conservative.

**Table 3.** Hyperfine structure constants of transitions of  $^{161}\text{Dy II}$  and  $^{163}\text{Dy II}$  where satellite peaks are not well fit.  $A$  and  $B$  are the magnetic dipole and electric quadrupole constants, respectively.  $J$  is the total angular momentum. Energies of odd-parity levels are italicized.

$\lambda_{\text{air}}^a$ (nm)	Configuration <sup>b</sup>	Term <sup>b</sup>	$J^b$	Energy <sup>b</sup> ( $\text{cm}^{-1}$ )	$A$ ( $^{161}\text{Dy}$ ) (MHz)	$B$ ( $^{161}\text{Dy}$ ) (MHz)	$A$ ( $^{163}\text{Dy}$ ) (MHz)	$B$ ( $^{163}\text{Dy}$ ) (MHz)
424.846	$4f^9(^6\text{H}^\circ)5d(^7\text{H}^\circ)6s$	$^8\text{H}^\circ$	11/2	<i>14,347.205</i>	−63.33 (91)	1905 (37)	88.7 (1.3)	2012 (39)
	$4f^9(^6\text{H}^\circ)6s6p(^3\text{P}^\circ)$		13/2	37,878.55	−26.0 (1.4)	1552 (31)	36.4 (2.0)	1639 (32)
436.135	$4f^9(^6\text{H}^\circ)5d(^7\text{I}^\circ)6s$	$^8\text{I}^\circ$	17/2	<i>14,895.06</i>	−94.86 (79)	2106 (60)	132.8 (1.1)	2224 (64)
	$4f^9(^6\text{H}^\circ)5d(^7\text{H}^\circ)6p$		15/2	37,817.31	−65.15 (91)	1598 (59)	91.2 (1.3)	1688 (62)
451.851	$4f^9(^6\text{H}^\circ)5d^2(^3\text{F})$	$^8\text{K}^\circ$	21/2	<i>22,031.98</i>	11.69 (73)	−1613 (50)	−16.4 (1.0)	−1704 (53)
	$4f^9(^6\text{H}^\circ)5d(^7\text{I}^\circ)6p$	$^8\text{K}$	21/2	44,156.98	−7.72 (73)	−503 (50)	10.8 (1.0)	−531 (53)
457.385	$4f^9(^6\text{H}^\circ)5d^2(^3\text{F})$	$^\circ$	17/2	<i>20,884.42</i>	68.32 (87)	−1358 (63)	−95.6 (1.2)	−1434 (66)
	$4f^9(^6\text{H}^\circ)5d(^7\text{H}^\circ)6p$		17/2	42,741.69	44.11 (88)	−1206 (63)	−61.7 (1.2)	−1274 (66)

<sup>a</sup> Reference [31]. <sup>b</sup> Reference [17].

**Table 4.** Isotope shifts in Dy II, denoted by mass pairs:  $(M, M')$ . The signs are determined by the convention that  $IS \equiv \nu_{M'} - \nu_M$  where  $M' > M$ .  $J_{\text{lo}}, E_{\text{lo}}$  and  $J_{\text{up}}, E_{\text{up}}$  are the total angular momentum and energy of the lower and upper levels of a transition, respectively.

$\lambda_{\text{air}}^a$ (nm)	$J_{\text{lo}}^a$	$E_{\text{lo}}^a$ ( $\text{cm}^{-1}$ )	$J_{\text{up}}^a$	$E_{\text{up}}^a$ ( $\text{cm}^{-1}$ )	(160, 164) (MHz)	(161, 164) (MHz)	(162, 164) (MHz)	(163, 164) (MHz)
422.203 *	15/2	4341.10	13/2	28,019.70	−610 (11)	−427 (10)	−306 (10)	−129 (10)
424.846 *	11/2	<i>14,347.21</i>	13/2	37,878.55	−960 (11)	−842 (11)	−456 (11)	−326 (10)
432.253 *	11/2	13,338.27	9/2	36,466.34	−1760 (11)	−1453 (10)	−857 (10)	−533 (10)
432.891	15/2	4341.10	15/2	27,435.12	−1204 (10)	−945 (10)	−591 (10)	−331 (10)
436.135 *	17/2	<i>14,895.06</i>	15/2	37,817.31	−1429 (10)	−1237 (11)	−694 (10)	−463 (11)
436.421	19/2	19,571.75	19/2	42,478.98	−1812 (10)	−1550 (10)	−870 (10)	−581 (10)
437.531	19/2	17,606.65	17/2	40,455.73	−108 (10)	−74 (10)	−52 (10)	−23 (10)
438.430 *	13/2	7485.12	13/2	30,287.36	−1457 (11)	−1175 (10)	−707 (10)	−408 (10)
451.851 *	21/2	22,031.98	21/2	44,156.98	−363 (10)	−334 (11)	−173 (10)	−133 (10)
454.167	19/2	19,571.75	17/2	41,583.90	−1759 (10)	−1506 (11)	−847 (10)	−565 (10)
457.385	17/2	20,884.42	17/2	42,741.69	−790 (11)	−700 (11)	−378 (10)	−272 (10)
459.178	11/2	20,517.39	13/2	42,289.33	−709 (11)	−628 (10)	−339 (10)	−244 (10)

<sup>a</sup> Reference [31]. \* These transitions contained unidentified blends whose relative intensities were  $<15\%$ . A spectrum at 443.100 nm contained a blend of two transitions of comparable relative intensity and could not be analyzed.

#### 4. Discussion and Conclusions

We have measured hfs parameters in 14 levels of Dy II, and effective hfs parameters in a further four transitions. There is no previous hfs data for these levels for comparison, but the very large magnitude of the electric quadrupole constants is consistent with measurements in Dy I [32]. Comparison with hfs measurements in isoelectronic  $^{159}\text{Tb I}$  is not useful as the electron configurations of the levels studied [33] are different from those in the present work, and also because the magnetic dipole and electric quadrupole moments are quite different from those of  $^{161}\text{Dy}$  and  $^{163}\text{Dy}$ .

Of the 12 transition ISs we measured, we can compare three with the data of Ahmad et al. [20] made with a Fabry-Perot spectrometer viewing a hollow-cathode discharge. As shown in Table 5, the agreement is excellent, and our results are more precise by an order of magnitude. None of the transitions measured by Aufmuth [19] overlap with our data.

**Table 5.** Comparison of IS measurements with previous work.

$\lambda_{\text{air}}$ (nm)	Mass Pair	IS (MHz)	
		This Work	Ahmad [20]
432.891	(160, 164)	−1204 (10)	−1268 (90)
436.421	(160, 164)	−1812 (10)	−1820 (90)
437.531	(160, 164)	−108 (10)	~0 (90)

Another check on our IS values is through the conventional King plot analysis [29] (Chapter 6). As a reference transition in the King plots, we used the 597.4 nm transition in Dy I, for which ISs have been measured [34,35] at a high accuracy (~2 MHz). Both fits were excellent straight lines (see Figure 3). That linearity reflects almost entirely the quality of *our* data since the errors we have ascribed to our IS measurements are about five times greater than those for the reference transition. This suggests that the uncertainty of 10 MHz that we have attached to our IS measurements to account for source-voltage drift and residual nonlinearity is conservative.

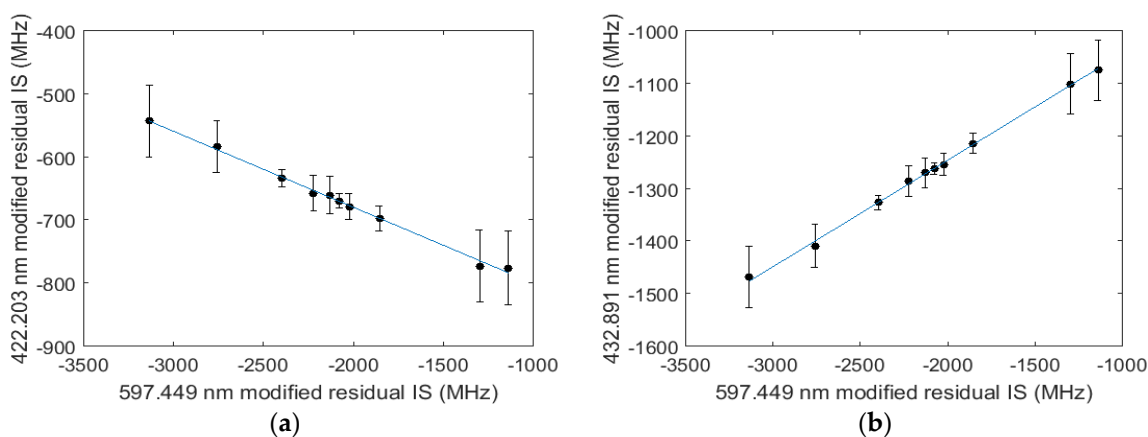


**Figure 3.** King plots of modified residual IS (see text) of pairs of transitions in Dy II and Dy I. The mass pair (160, 164) has been chosen as the reference, and points have been plotted for all unique pairs of isotopes. The straight line (blue online) is a linear least-squares fit. Note that the error bars in the horizontal direction are smaller than the data symbols. (a) King plot for the 422.201 nm vs. 597.449 nm transitions; (b) King plot for the 432.891 nm vs. 597.449 nm transitions.

**Acknowledgments:** We thank the Natural Sciences and Engineering Research Council of Canada for financial support. We thank Timothy J. Scholl for extremely helpful assistance with the laser system.

**Author Contributions:** All authors contributed equally to acquiring and analyzing data and writing the manuscript.

**Conflicts of Interest:** The authors declare no conflict of interest.

## References

1. Abt, A. Hyperfine structure in the solar spectrum. *Astrophys. J.* **1952**, *115*, 199–205. [[CrossRef](#)]
2. Jomaron, C.M.; Dworetsky, M.M.; Allen, C.S. Manganese abundances in mercury-manganese stars. *Mon. Not. R. Astron. Soc.* **1999**, *303*, 555–564. [[CrossRef](#)]
3. Kurucz, R.L. Atomic data for interpreting stellar spectra: Isotopic and hyperfine data. *Phys. Scr.* **1993**, *T47*, 110–117. [[CrossRef](#)]
4. Cowley, C.R. Lanthanide rare earths in stellar spectra with emphasis on chemically peculiar stars. *Phys. Scr.* **1984**, *T8*, 28–38. [[CrossRef](#)]
5. Sneden, C.; Cowan, J.J.; Gallino, R. Neutron-capture elements in the early Galaxy. *Ann. Rev. Astron. Astrophys.* **2008**, *46*, 241–288. [[CrossRef](#)]

6. Aoki, W.; Ryan, S.G.; Norris, J.E.; Beers, T.C.; Ando, H.; Iwamoto, N.; Kajino, T.; Mathews, G.J.; Fujimoto, M.Y. Neutron Capture Elements in s-Process-Rich, Very Metal-Poor Stars. *Astrophys. J.* **2001**, *561*, 346–363. [[CrossRef](#)]
7. Christlieb, N.; Beers, T.C.; Barklem, P.S.; Bessell, M.; Hill, V.; Holmberg, J.; Horn, A.J.; Marsteller, B.; Mashonkina, L.; Qian, Y.-Z.; et al. The Hamburg/ESO R-process Enhanced Star survey (HERES). I. Project description, and discovery of two stars with strong enhancements of neutron-capture elements. *Astron. Astrophys.* **2004**, *428*, 1027–1037. [[CrossRef](#)]
8. François, P.; Depagne, E.; Hill, V.; Spite, M.; Spite, F.; Plez, B.; Beers, T.C.; Andersen, J.; James, G.; Barbuy, B.; et al. First stars. VIII. Enrichment of the neutron-capture elements in the early Galaxy. *Astron. Astrophys.* **2007**, *476*, 935–950. [[CrossRef](#)]
9. Burris, D.L.; Pilachowski, C.A.; Armandroff, T.E.; Sneden, C.; Cowan, J.; Roe, H. Neutron-capture elements in the early Galaxy: Insights from a large sample of metal-poor giants. *Astrophys. J.* **2000**, *544*, 302–319. [[CrossRef](#)]
10. Karinkuzhi, D.; Goswami, A. Chemical analysis of CH stars—II. Atmospheric parameters and elemental abundances. *Mon. Not. R. Astron. Soc.* **2015**, *446*, 2348–2362. [[CrossRef](#)]
11. Chaplin, W.J.; Miglio, A. Asteroseismology of Solar-Type and Red-Giant stars. *Ann. Rev. Astron. Astrophys.* **2013**, *51*, 353–392. [[CrossRef](#)]
12. Conway, J.G.; Worden, E.F. Preliminary level analysis of the first and second spectra of dysprosium, Dy I and Dy II. *J. Opt. Soc. Am.* **1971**, *61*, 704–726. [[CrossRef](#)]
13. Wyart, J.F. Interpretation du spectre de Dy II. I. Etude des configurations impaires. *Physica* **1972**, *61*, 182–190. [[CrossRef](#)]
14. Wyart, J.F. Interpretation du spectre de Dy II. II. Etude des configurations  $4f^9 6s 6p$  ET  $4f^9 5d 6p$ . *Physica* **1972**, *61*, 191–199. [[CrossRef](#)]
15. Wyart, J.F. Interprétation du spectre de Dy II. III. Etude des configurations  $4f^{10} 6s$  ET  $4f^{10} 5d$ . *Physica B+C* **1976**, *83*, 361–366. [[CrossRef](#)]
16. Nave, G.; Griesmann, U. New energy levels and classifications of spectral lines from neutral and singly-ionized dysprosium (Dy I and Dy II). *Phys. Scr.* **2000**, *62*, 463–473. [[CrossRef](#)]
17. Kramida, A.; Ralchenko, Y.; Reader, J.; NIST ASD Team. *NIST Atomic Spectra Database*; version 5.4; National Institute of Standards and Technology: Gaithersburg, MD, USA, 2016. Available online: <http://physics.nist.gov/asd> (accessed on 9 January 2017).
18. Pacheva, Y.; Abadjieva, L. ИЗОТОПИНО ОТМЕСТВАНЕ В СПЕКТЪРА НА ДИСПРОЗИЯ. *Bull. de l'Institut de Physique et de Recherche Atomique (Bulgaria)* **1968**, *17*, 87–93. (In Bulgarian)
19. Aufmuth, P. Isotope shift and configuration mixing in dysprosium II. *Z. Phys. A* **1978**, *286*, 235–241. [[CrossRef](#)]
20. Ahmad, S.A.; Venugopalan, A.; Saksena, G.D. Electronic configuration mixing and isotope shifts in singly ionized dysprosium. *Spectrochim. Acta* **1983**, *38B*, 1115–1124. [[CrossRef](#)]
21. Murakawa, K.; Kamei, T. Hyperfine structure of the spectra of dysprosium, cobalt, vanadium, manganese, and lanthanum. *Phys. Rev.* **1953**, *92*, 325–327. [[CrossRef](#)]
22. Demtröder, W. *Laser Spectroscopy*, 5th ed.; Springer: Berlin, Germany, 2015; Volume 2, pp. 208–211.
23. Kaufman, S.L. High-resolution laser spectroscopy in fast beams. *Opt. Commun.* **1976**, *17*, 309–312. [[CrossRef](#)]
24. Nouri, Z.; Li, R.; Holt, R.A.; Rosner, S.D. A Penning sputter ion source with very low energy spread. *Nucl. Instrum. Methods Phys. Res. A* **2010**, *614*, 174–178. [[CrossRef](#)]
25. Nouri, Z.; Li, R.; Holt, R.A.; Rosner, S.D. Corrigendum to “A Penning sputter ion source with very low energy spread” [Nuclear Instr. and Meth. A 614 (2010) 174–178]. *Nucl. Instrum. Methods Phys. Res. A* **2010**, *621*, 717. [[CrossRef](#)]
26. Audi, G.; Wapstra, A.H.; Thibault, C. The AME2003 atomic mass evaluation. (II). Tables, graphs and references. *Nucl. Phys. A* **2003**, *729*, 337–676. [[CrossRef](#)]
27. De Bièvre, P.; Taylor, P.D.P. Table of the isotopic compositions of the elements. *Int. J. Mass Spectrom. Ion Proc.* **1993**, *123*, 149–166. [[CrossRef](#)]
28. Holden, N.E. Table of the isotopes. In *CRC Handbook of Chemistry and Physics*, 97th ed.; CRC Press: Boca Raton, FL, USA, 2016; p. 263. Available online: [http://hbcponline.com/faces/documents/11\\_02/11\\_02\\_0263.xhtml](http://hbcponline.com/faces/documents/11_02/11_02_0263.xhtml) (accessed on 17 January 2017).
29. Hall, J.L.; Lee, S.A. Interferometric real-time display of CW dye laser wavelength with sub-Doppler accuracy. *Appl. Phys. Lett.* **1976**, *29*, 367–369. [[CrossRef](#)]

30. Woodgate, G.K. *Elementary Atomic Structure*, 2nd ed.; Clarendon: Oxford, UK, 1980; p. 184.
31. Kurucz, R.L.; Bell, B. *Atomic Line Data*; Kurucz CD-ROM No. 23; Cambridge, Mass: Smithsonian Astrophysical Observatory: Cambridge, MA, USA, 1995.
32. Childs, W.J.; Crosswhite, H.; Goodman, L.S.; Pfeufer, V. Hyperfine structure of  $4f^N 6s^2$  configurations in  $^{159}\text{Tb}$ ,  $^{161,163}\text{Dy}$ , and  $^{169}\text{Tm}$ . *J. Opt. Soc. Am. B* **1984**, *1*, 22–29. [[CrossRef](#)]
33. Childs, W.J. Hyperfine Structure of Many Atomic Levels of  $\text{Tb}^{159}$  and the  $\text{Tb}^{159}$  Nuclear Electric-Quadrupole Moment. *Phys. Rev. A* **1970**, *2*, 316–336. [[CrossRef](#)]
34. Dekker, J.W.M.; Klinkenberg, P.F.A.; Langkemper, J.F. Optical isotope shifts and nuclear deformation in dysprosium. *Physica* **1968**, *39*, 393–412. [[CrossRef](#)]
35. Wakasugi, M.; Horiguchi, T.; Jin, W.G.; Sakata, H.; Yoshizawa, Y. Changes of the Nuclear Charge Distribution of Nd, Sm, Gd and Dy from Optical Isotope Shifts. *J. Phys. Soc. Jpn.* **1990**, *59*, 2700–2713. [[CrossRef](#)]



© 2017 by the authors; licensee MDPI, Basel, Switzerland. This article is an open access article distributed under the terms and conditions of the Creative Commons Attribution (CC BY) license (<http://creativecommons.org/licenses/by/4.0/>).